Current Applied Physics 18 (2018) 785–792

Contents lists available at ScienceDirect

Current Applied Physics

journal homepage: www.elsevier.com/locate/cap

Waveguiding behavior of VLS-grown one-dimensional Ga-doped In_2O_3 nanostructures

Jesús Alberto Ramos Ramón[a], U. Pal[a,*], David Maestre[b], Ana Cremades[b]

[a] Instituto de Física, Benemérita Universidad Autónoma de Puebla, Apdo. Postal J-48, Puebla, Pue, 72570, Mexico
[b] Departamento de Física de Materiales, Facultad de Ciencias Físicas, Universidad Complutense de Madrid, 28040, Madrid, Spain

ARTICLE INFO

Keywords:
In_2O_3 nanorods
Ga-incorporation
Waveguiding behavior
Resonant microcavities

ABSTRACT

Highly crystalline undoped and Ga-doped indium oxide nanorods with square-shaped faceted morphology were fabricated through the vapor-liquid-solid process at moderate temperature. Effects of Ga incorporation on the growth rate, morphology, and crystallinity of the nanostructures were evaluated by scanning electron microscopy, transmission electron microscopy, and X-ray diffraction. Defect structure and waveguiding behavior of the 1-D In_2O_3 nanostructures have been studied using microRaman and micro photoluminescence spectroscopies. The appearance of several resonant modes superposed over the broad room temperature micro-photoluminescence spectra of the nanostructures demonstrates their waveguiding behaviors. While the pristine or undoped In_2O_3 nanostructures of 20–150 nm widths revealed Fabry-Pérot resonance modes, the Ga-incorporated nanostructures of 20–100 nm width revealed whispering gallery modes due to their smaller widths. The quality factor (Q) of the resonators was estimated to be about 20.86 and 188.79 for the pristine and Ga-incorporated nanostructures, respectively, indicating a huge enhancement due to Ga incorporation. The increment in the Q factor on Ga incorporation in In_2O_3 nanorods opens up the possibility of their utilization for the development of new optical transmitters and resonators, and fabrication of nanoscopic lasing devices.

1. Introduction

Progress in microelectronics has made a huge technological advancement in the last decades through the development of micron and sub-micron sized devices. However, the limited transmission bandwidth and the energy loss due to electrical resistance are still the problems for most of the optical communication devices, even though the conductivity of a material can be improved by incorporating defects or foreign elements. To overcome these constraints, fabrication of optical-transmission materials at micro- and nanoscales using different physical and chemical growth techniques have shown to be promising, as they can be used as building blocks for efficient light propagation [1], especially for applications in communications [2], or optical computers [3]. Investigations on the waveguiding behavior of different transparent metallic oxides, such as GeO_2 [4], SnO_2 [5], and Ga_2O_3 [6], have been successfully carried out to develop new optical transmission conducts. While these materials have high light transmission capacity, they can be prepared using simple fabrication methods, which is very important for the development of large-scale production of optoelectronic devices. In this context, indium oxide (In_2O_3) has been synthesized by different physical and chemical processes [7–9] with high yields, and utilized in several applications as the building blocks for the fabrication of new artificial, size and shape-tuned nano- and microscopic structures, which are also excellent candidates for the fabrication and betterment of several optoelectronic devices such as UV light emitters [9], solar cells [10], and field effect transistors [11]. As In_2O_3 is a wide band gap semiconductor (3.5–3.7 eV) with excellent optical transmittance and good chemical stability, its optical properties have been extensively studied, specifically its optical absorption [12], photo- [13], and cathodoluminescence [14] behaviors. Nevertheless, despite the high refractive index of In_2O_3 ($\sim$2.0) [15], the possible applications of In_2O_3 nano- and microstructures as waveguide and light manipulator have received much less attention [16,17].

In this article, we report on the fabrication of 1D pristine and Ga-incorporated In_2O_3 nanostructures grown by vapor-liquid-solid (VLS) process and their waveguiding behaviors. Apart from analyzing the morphology, composition, and crystalline quality of the nanostructures, the effect of Ga-incorporation on the waveguiding behavior of the fabricated nanostructures have been studied.

* Corresponding author.
E-mail address: upal@ifuap.buap.mx (U. Pal).

https://doi.org/10.1016/j.cap.2018.04.009
Received 14 January 2018; Accepted 9 April 2018
Available online 12 April 2018

2. Materials and methods

Pristine and Ga-incorporated In_2O_3 nanostructures were fabricated through VLS in a horizontal quartz tube furnace. For Ga-incorporated samples, metallic indium (drops, ~2 mm diameter, Sigma Aldrich, 99.98%) and gallium (splatter, Sigma Aldrich, 99.99%) were mixed with graphite powder in In:Ga:C nominal weight ratio of 5:1:3 and put into a quartz crucible. Silicon substrates covered with sputter-deposited Au thin film (~20 nm) were set face down over the crucible to reduce the distance between the substrate and the reactants. For comparison, In_2O_3 nanostructures without Ga (designated as pristine nanostructures) were also fabricated following the same procedure, utilizing only indium and graphite in the precursor mixture, keeping their weight ratio fixed (5:3). The precursor and substrate loaded crucible was put at the maximum temperature zone (center) of the furnace. The quartz tube was sealed at both ends with metallic flanges and Ar (99.996% purity) gas was flown for about 30 min to eliminate residual air from the chamber. Then the furnace was heated up to 900 °C with a heating rate of 37 °C/min under an Ar + O_2 (99.999% purity) gas mixture flow (10:1 v/v, 66 sccm). Keeping at maximum temperature for 15 min, the furnace was naturally cooled down to room temperature. In order to analyze the obtained nanostructures, the yellowish products deposited over Si substrate were gently removed by scratching and deposited on fresh silicon substrates. A JEOL JSM 7800 F field-emission scanning electron microscope (FESEM) was utilized to observe the morphology of the as-grown nanostructures. Elemental composition of the pristine and Ga-incorporated nanostructures was analyzed with an Oxford X-Max analytical system attached to the FESEM. Crystal quality, waveguiding behavior, and optical resonance of the nanostructures were analyzed through room temperature microRaman (μRaman) spectroscopy, optical imaging, and micro-photoluminescence (μPL) spectroscopy, respectively, in a Horiba LabRam HR system, utilizing a 633 nm He-Ne and a 325 nm He-Cd lasers, a thermoelectrically cooled charge-coupled device (CCD) detector, and an Olympus BX confocal microscope with 40× and 100× objective lenses to concentrate the incident laser beam. The experimental setup used for the waveguiding tests, μPL and μRaman analysis of the pristine and Ga-incorporated nanostructures is shown schematically in Fig. 1. For structural and defects distribution study in the nanostructures, a JEOL JEM 2100 transmission electron microscope operating at 200 kV was utilized. For the analysis of chemical state of the constituting elements, a Thermo Scientific X-ray photoelectron spectrometer (XPS), equipped with Al Kα X-ray source (1486.6 eV) was utilized. Binding energy of each of the elements was calibrated using C1s energy position at 284.6 eV.

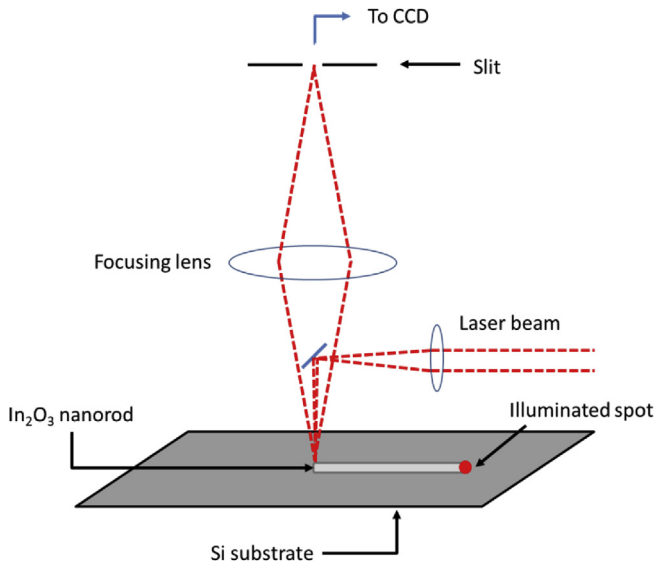

Fig. 1. Schematic illustration of the setup used for μPL, μRaman, and waveguiding characterizations of the fabricated nanostructures.

3. Results and discussion

Fig. 2a and b show the typical morphology of the pristine and Ga-incorporated In_2O_3 nanostructures. From the SEM images, while the dimensions most of the nanostructures were estimated to be in-between 0.7 - 2.0 μm in length and 20–150 nm in width for the pristine In_2O_3 nanostructures, a few grew over 10 μm. On the other hand, most of the Ga-incorporated nanostructures were of 2.0–10.0 μm in length and 20–100 nm in width. Nevertheless, some of the Ga-incorporated nanostructures grew over tens of microns (e.g. one shown in Fig. 7c), clearly indicating an enhancement in growth rate due to Ga incorporation. While most of the nanorods of the pristine sample have tapered ends (Fig. 2c), the nanorods of the Ga-doped sample are usually straight, without tapered ends (Fig. 2d); obviously attached with catalyst particles. The tapered growth of pristine In_2O_3 nanorods is due to the difference in growth time between the base of the rods and their tips. While these nanorods were grown by VLS process, an unavoidable VS growth process occurs at their lateral faces simultaneously [18]. The growth rate enhancement of the In_2O_3 nanostructures due to Ga incorporation reduces the tapering effect and surface roughness of the nanorods. As can be observed in the SEM micrographs, the surface of some of the pristine In_2O_3 nanostructures contain staircase-like steps (Fig. 2c), probably due to fluctuation in the growth conditions [19].

Fig. 2e shows typical EDS spectra of the pristine and Ga-incorporated samples measured on isolated rods deposited on silicon substrates. For the pristine sample, estimated elemental compositions for In and O were 68.9 at.% and 31.1 at.%, respectively. The strong Si signal appeared around 1.74 eV for the pristine sample is from the Si substrate utilized as support. For the Ga-incorporated sample, the additional signal of L_α line of Ga appeared. Quantitative EDS analysis of the sample revealed 27.1, 70.8, and 2.1 at.% of In, O, and Ga, respectively. As can be noticed, the EDS estimated Ga content in the sample is much lower than its nominal value, probably due to the difference in vapor pressure of In and Ga [20] and low solubility of Ga in In_2O_3 [21]. Absence of additional peaks associated to other elements indicates a high purity of the fabricated nanostructures.

Transversal EDS profile of single In_2O_3 and Ga-incorporated In_2O_3 nanostructures were recorded through linear scans. In Fig. 3, single nanostructures of pristine and Ga-incorporated samples and their respective EDS elemental profile are displayed, where the homogeneous distribution of In and O elements can be observed in both the cases. On the other hand, the spatial distribution of Ga in the Ga-incorporated nanostructure revealed a higher Ga concentration at its edges. The higher concentration of Ga at the nanorod surface is caused by an out-diffusion process, which often takes place in the fabrication of doped metal-oxide semiconductor nanostructures [22].

Room temperature Raman spectra of the pristine and Ga-incorporated nanorods were acquired in 100–700 cm^{-1} range to analyze the effect of Ga incorporation into the lattice structure of the In_2O_3 nanocrystals (Fig. 4). Raman spectra of the pristine nanostructures revealed six vibrational modes at 108 ($T_g^{(1)}$), 130 ($A_g^{(1)}$), 305 ($T_g^{(2)}$), 365 ($T_g^{(3)}$), 495 ($A_g^{(2)}$) and 627 cm^{-1} ($A_g^{(3)}$), all corresponding to the In_2O_3 lattice in cubic phase [23]. All these vibrational modes were also revealed for the Ga-incorporated nanorods. However, the bands in this case are slightly broader, probably due to a mild lattice distortion due to Ga incorporation. As the intensity of the vibrational bands did not change significantly due to Ga incorporation, the crystalline quality of the Ga-incorporated In_2O_3 nanorods can be considered as good as the pristine samples.

Effect of Ga incorporation in the lattice of In_2O_3 nanorods was analyzed further through TEM analysis. The high crystalline quality of the pristine nanorods (Fig. 5a) can be seen in the HRTEM image presented in Fig. 5b. The nanostructures grew preferentially along [100]

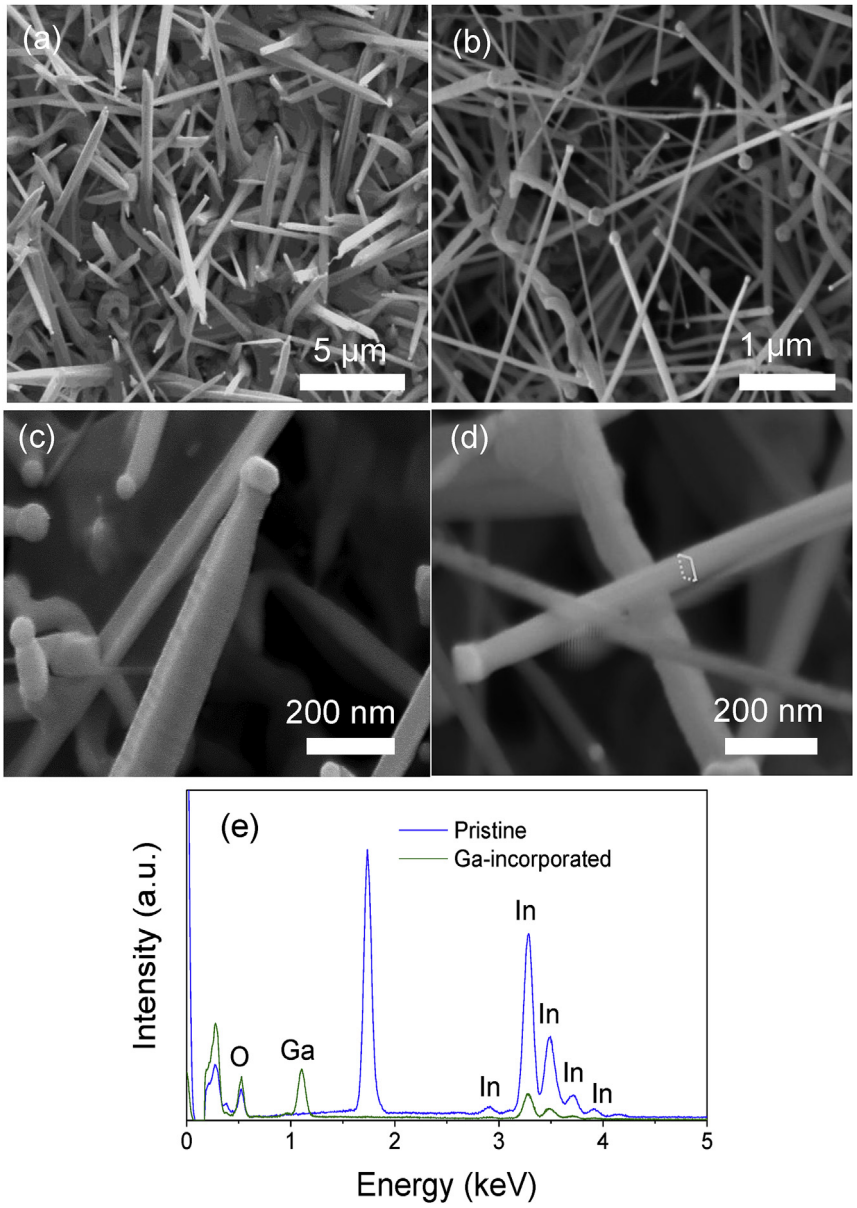

Fig. 2. Typical SEM images of the fabricated (a) pristine and (b) Ga-incorporated In_2O_3 nanostructures. Amplified SEM images of single (c) pristine and (d) Ga-incorporated structures show their square-like cross-section; (e) EDS spectra of pristine and Ga-incorporated In_2O_3 nanostructures.

direction, with an interplanar spacing close to the (400) standard interplanar spacing of In_2O_3 in cubic phase (JPCDS no. 06-0416). While the formation of longer nanorods in the Ga-incorporated sample is very clear from the SEM images of the sample, the formation of a few core-shell structures (Fig. 5c) in the sample could be observed in its TEM images. Formation of such core-shell structures in the sample indicates a segregation of Ga towards nanorod surface due to the low solubility of Ga in In_2O_3 and the slower evaporation rate of Ga compared to In, as mentioned earlier. The high-resolution TEM image of the Ga-incorporated nanorod presented in Fig. 5d indicates the persistence of their high crystallinity even after Ga incorporation. While there was no change in the growth direction of In_2O_3 nanorods due to Ga incorporation, the formation of β-Ga_2O_3 clusters near the surface of the nanorods was detected in their HRTEM images; validating the EDS results obtained earlier (Fig. 3d).

XPS analysis was carried out on the pristine and Ga-incorporated samples to confirm the presence of Ga and its oxidation state in the Ga-incorporated nanostructures (Fig. 6), considering XPS is a powerful technique for surface analysis. The spectra were calibrated using the C *1s* peak from adventitious carbon at 284.6 eV. As can be seen in Fig. 6, the survey spectrum of the pristine sample (upper spectrum) revealed only the presence of In and O, while the Ga-incorporated sample revealed Ga core-level emissions along with the emissions of In and O. XPS estimated elemental composition obtained for the Ga-incorporated samples was 6.42, 36.43 and 57.15 at. % for In, O, and Ga, respectively. As can be noticed, the XPS estimated elemental composition of the sample is quite different from the ESD estimated composition. Typically, the penetration depth of the X-ray in XPS analysis is ~10 nm from the surface of a sample, while in EDS analysis, the penetration depth of electrons vary from hundreds of nanometers to a few microns, depending on the applied accelerating voltage (for 20 kV, the depth penetration is around 1 μm). A huge enhancement in the Ga concentration in XPS analysis clearly indicates the segregation of incorporated Ga towards the surface of the nanostructures. In fact, the result revalidates the results obtained from the EDS profiles (Fig. 3) measured across the lateral sections of the nanostructures.

Optical images of nanostructures illuminated with white light from a halogen lamp and irradiated with He-Ne laser spot are shown in

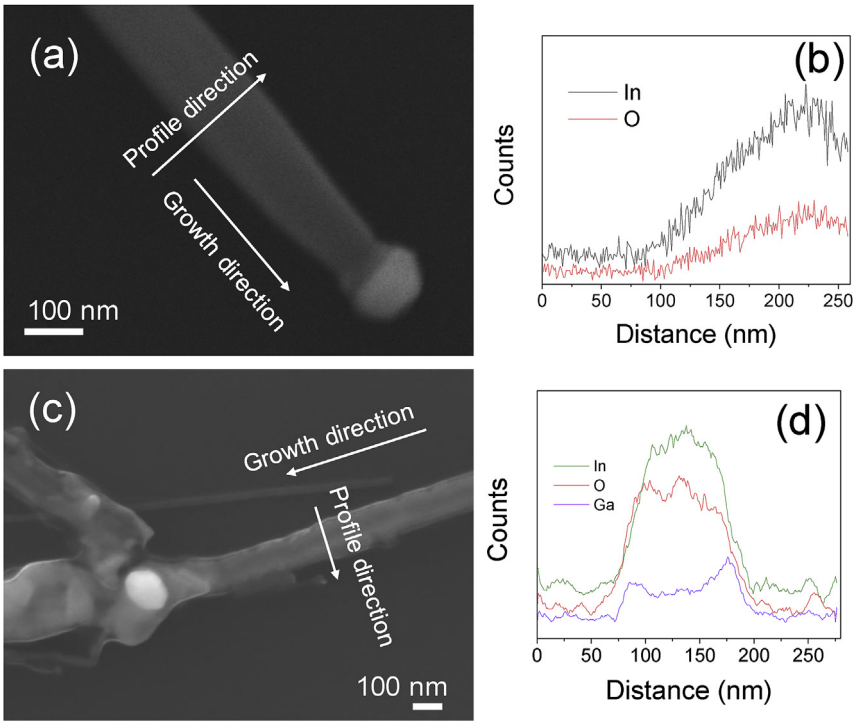

Fig. 3. Typical SEM images and corresponding EDS profiles of single (a, b) pristine and (c, d) Ga-incorporated In_2O_3 nanorods measured along their cross-sections.

Fig. 7. To probe the waveguiding behavior of pristine and Ga-incorporated nanorods, a He-Ne laser beam (633 nm) was vertically projected to one end of a nanorod (see Fig. 1). Optical images of the nanostructures under white light illumination (Fig. 7a and c) revealed both the pristine and Ga-incorporated In_2O_3 nanostructures are transparent in the visible light, as expected for In_2O_3, which is a wide band gap semiconductor. Despite a major part of the incident laser beam was scattered by the nanorods (Fig. 7b and d), a small fraction was transmitted along the nanorods. On illuminating the pristine nanostructures with 633 nm laser beam (Fig. 7b) at one end, the whole structure remained invisible, transmitting almost all the light to its other end. However, a fraction of the incident light is scattered from the surface of the nanostructures. In a similar fashion, for the Ga-incorporated nanorods (Fig. 7d), the incident laser beam is transmitted along the

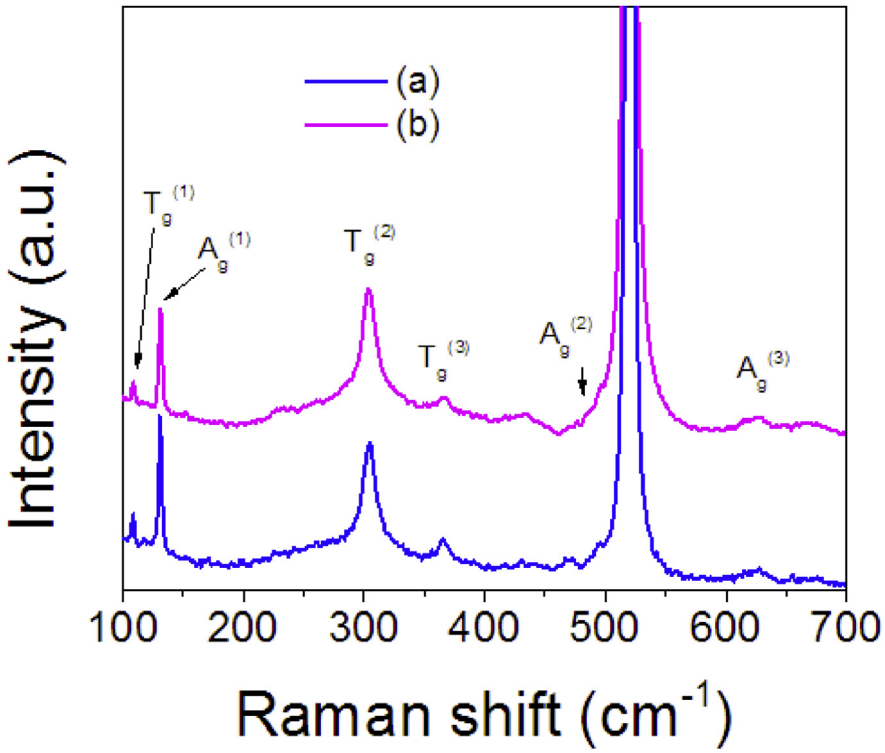

Fig. 4. Raman spectra of typical (a) pristine and (b) Ga-incorporated In_2O_3 nanostructures. The vibrational mode at 520 cm^{-1} corresponds to the TO mode of the Si wafer used as substrate.

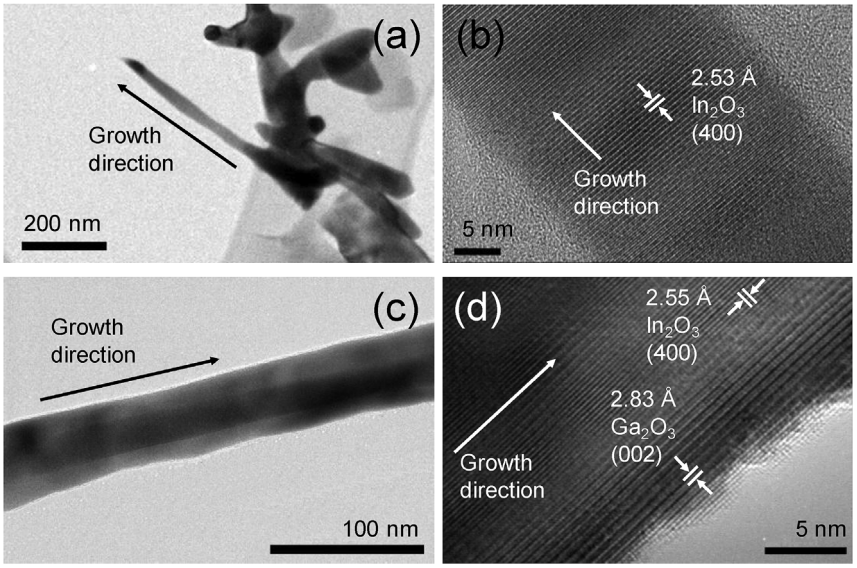

Fig. 5. Typical TEM and HRTEM images of (a, b) pristine, and (c, d) Ga-incorporated In_2O_3 nanorods. Formation of core-shell structure due to Ga-incorporation in high concentration in In_2O_3 nanorods is very clear in (c).

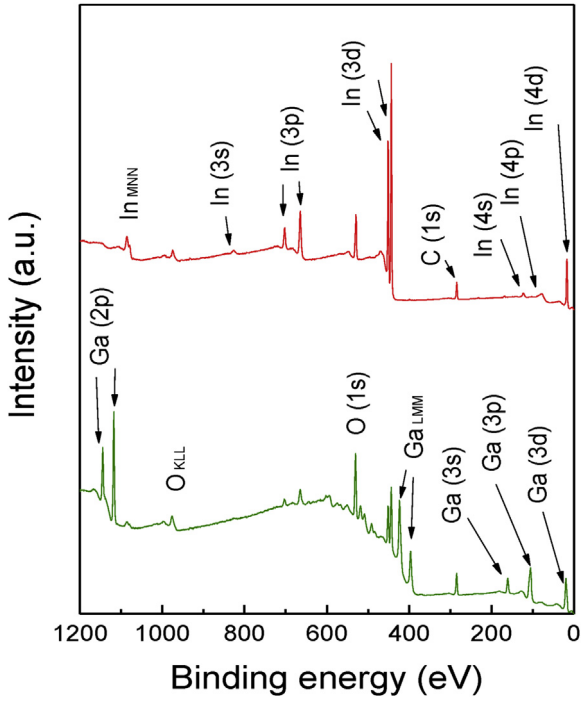

Fig. 6. XPS survey spectra of the pristine (upper) and Ga-incorporated (lower) In_2O_3 nanostructures.

nanorod with even lower scattering from their surface. The higher surface roughness of the pristine nanorods might be the reason for higher light scattering from their surface. It is important to mention at this point that not all the nanorods, either pristine or Ga-incorporated, present waveguiding behavior. The waveguiding property depends on the effective surface area irradiated by the light source, the incident irradiation angle, and the dimension of the nanostructure, as has been observed by Nogales et al. for Cr-doped Ga_2O_3 [6].

Room temperature microphotoluminescence spectra of the pristine and Ga-incorporated nanostructures were acquired perpendicular to their growth axis in the 320–760 nm spectral range, using a He-Cd laser beam ($\lambda = 325$ nm). Acquired μPL spectra of the pristine and Ga-incorporated In_2O_3 nanorods, shown in the corresponding insets, are presented in Fig. 8. The pristine nanostructures present a broad emission around 680 nm (Fig. 8a), which is frequently associated with oxygen defects such as oxygen vacancies (V_O) [24]. However, through electron spin resonance (ESR) spectroscopy, Kumar et al. [13] have recently demonstrated these emissions can be can be associated to In^{3+} interstitials in In_2O_3 nanoparticles. On the other hand, Ga-incorporated nanostructures show a broad strong emission around 600 nm with a less intense emission at about 690 nm. The emission at ~600 nm might be the result of radiative recombination of a photoexcited electron in singly-ionized V_O sites, as observed in the photoluminescence emission of ZnO nanostructures [25,26].

In the μPL spectra of pristine and Ga-incorporated In_2O_3 nanorods (Fig. 8a and b) appearance of resonant modes is observed. Since all the μPL measurements were carried out at room temperature, the appearance of multiple excitonic modes can be ruled out. Besides, the Bohr excitonic radius for In_2O_3 is ~2.38 nm [27] and the dimensions of the fabricated nanostructures are much larger, so the quantum confinement effect on the μPL emissions cannot be present. Therefore, the oscillations present in the pristine and Ga-incorporated μPL spectra are associated with a different process. For the pristine In_2O_3 nanorods, the resonant modes can be associated with a Fabry-Pérot resonance. The resonance condition can be reached when the optical path (product of nanorods refractive index (n) and the size of the optical cavity (L_{FP})) is N times the resonance wavelength (λ); where N is an integer (Eq. (1)):

$$N\lambda = nL_{FP} \tag{1}$$

Thus, the separation of Fabry-Pérot resonance peaks ($\Delta\lambda$) is given by

$$\Delta\lambda = \frac{\lambda^2}{L_{FP}\left(n - \lambda\frac{dn}{d\lambda}\right)} \tag{2}$$

where the term $\left(n - \lambda\frac{dn}{d\lambda}\right)$ is the group refractive index (n_g). Utilizing equation (1), the estimated average cavity size for the pristine nanorods at $\lambda = 705$ nm could be estimated about 1245 nm for a refractive index $n = 1.97$. The refractive index n was calculated from the Cauchy dispersion equation $n = A + B/\lambda^2$, with $A = 1.85$ and $B = 59205.92\ \text{nm}^2$ for In_2O_3 [28].

The obtained value of $L_{FP} = 2d$, where d is the cavity size (in this case, the nanorod width), is well consistent with the measured width of the rod from its optical image (~1240 ± 150 nm, Fig. 7a), which confirms the formation of a Fabry-Pérot type optical cavity (Fig. 8c). However, for the Ga-incorporated nanorod, the value (~1020 nm) of

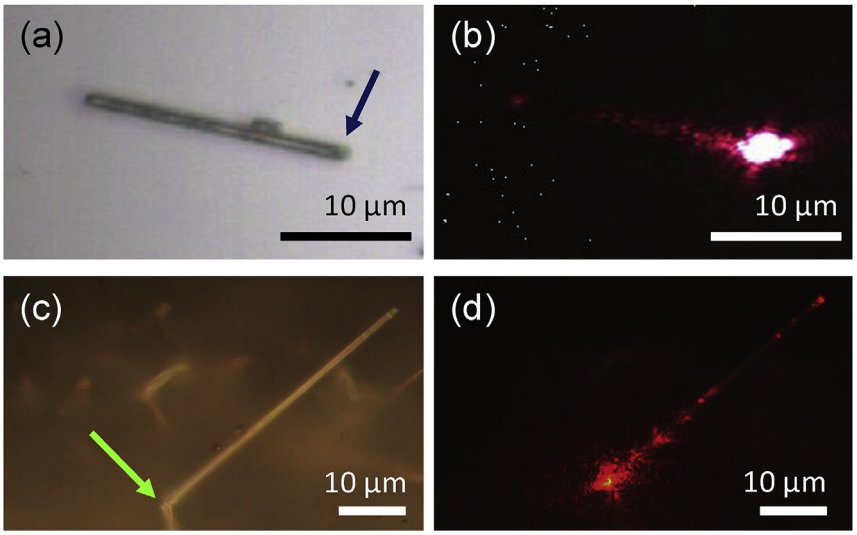

Fig. 7. Optical images of (a) pristine and (c) Ga-incorporated nanorods and their waveguide behavior ((b) and (d), respectively). It is observed that the laser light beam is transmitted along the nanostructures. The arrows in (a) and (c) indicate the point of illumination for each of the nanorods.

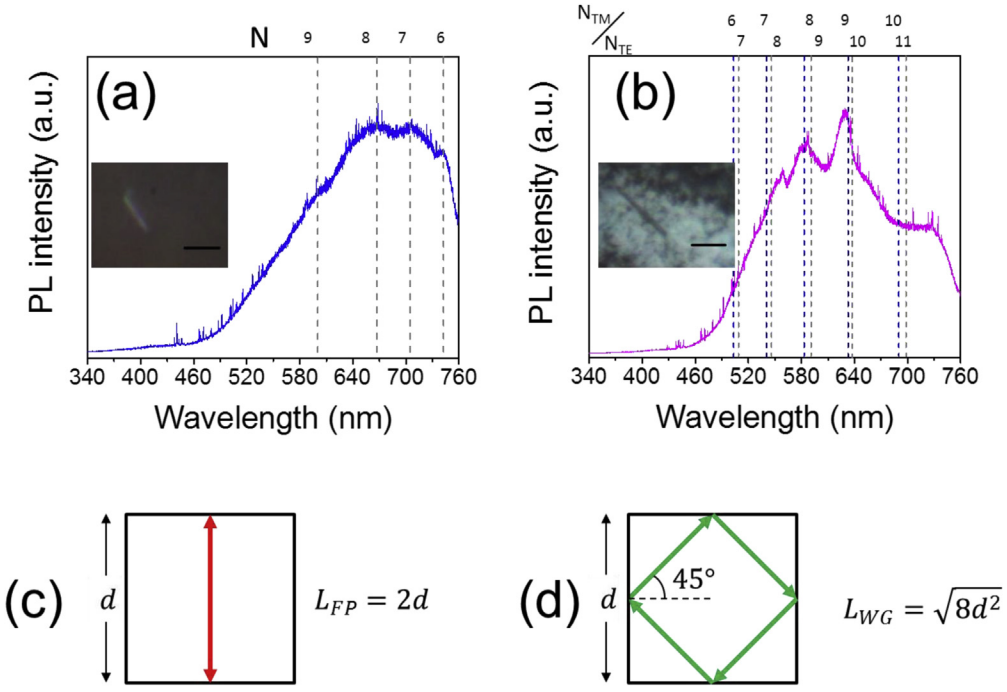

Fig. 8. Representative µPL spectra of (a) pristine and (b) Ga-incorporated nanorods (inset, scale bar = 10 µm) showing resonant peaks and their calculated position for TE and TM polarizations. There are two possible types of resonance (c) Fabry-Pérot and (d) Whispering-Gallery modes and their respective optical paths L_{FP} and L_{WG} in the cross section of a nanorod with width d according to the plane wave model.

estimated cavity length from the µPL spectrum (Fig. 8b) does not agree with the measured average width of the nanorod. Utilizing the estimated average width of the nanorod in equation (2) as cavity size, we could estimate a refractive index for the Ga-incorporated nanorod about 3.0, which is much higher than the reported refractive index of In_2O_3 (~2.0) [15]. Such a discrepancy indicates the involvement of a different type of interaction in the PL resonances in Ga-incorporated In_2O_3 nanorods.

Another type of resonance frequently observed in metal-oxide semiconductor is the resonance associated with whispering gallery mode, which is an electromagnetic resonance corresponding to the total internal reflection of trapped light from the surface in circular paths [29]. The resonance condition for whispering gallery modes can be described in the frame of classical electrodynamics, using a plane wave model, considering an optical cavity with dimensions higher than the wavelength of the confined light [5,17]. In this model, the resonance condition is given by a phase shift (δ) each time the plane wave is reflected by the cavity, which can be separated in two components depending on polarization (Eq. (3)):

$$\delta_{TE} = -2\arctan\left(n^2\sqrt{\frac{\sin^2\theta_i - \frac{1}{n^2}}{\cos^2\theta_i}}\right) \tag{3a}$$

$$\delta_{TM} = -2\arctan\left(\sqrt{\frac{\sin^2\theta_i - \frac{1}{n^2}}{\cos^2\theta_i}}\right) \tag{3b}$$

where θ_i is the incidence angle and n is the refractive index. Sub-indexes

TE and TM stand for the cases when the electric field component of the incident plane wave is parallel and perpendicular to the incident plane, respectively [17]. The equations for the whispering gallery resonance wavelength for each polarization are then:

$$\lambda_{TE} = \frac{nL_{WG}}{N - \frac{m}{2} + \frac{m}{\pi}\left[2\arctan\left(n^2\sqrt{\frac{\sin^2\theta_i - \frac{1}{n^2}}{\cos^2\theta_i}}\right)\right]} \quad (4a)$$

$$\lambda_{TM} = \frac{nL_{WG}}{N + \frac{m}{\pi}\left[2\arctan\left(\sqrt{\frac{\sin^2\theta_i - \frac{1}{n^2}}{\cos^2\theta_i}}\right)\right]} \quad (4b)$$

with m the total number of reflections in one lap. Since the cross section of these nanorods was of square shape, an incident angle of approximately 45° can considered for total internal reflection, and hence Eqs. (4a) and (4b) can be rewritten as:

$$\lambda_{TE} = \frac{nL_{WG}}{N - 2 + \frac{4}{\pi}[\arctan(n\sqrt{n^2 - 2})]} \quad (5a)$$

$$\lambda_{TM} = \frac{nL_{WG}}{N + \frac{4}{\pi}\left[\arctan\left(\frac{1}{n}\sqrt{n^2 - 2}\right)\right]} \quad (5b)$$

From Eq. (5), the refractive index can be estimated for integer values of N and the λ vales of the μPL spectrum. For example, for a nanorod of width d= 1020 ± 70 nm, the optical path L_{WG} is 2890 ± 200 nm. Then, the refractive index was varied until the wavelength values for both polarizations matched with the observed resonances in the μPL spectrum, giving a value of 2.08. Despite that in $GaInO_3$ thin films the refractive index obtained through optical measurements is 1.65 [30], the most common values of reported refractive index for In and Ga oxide systems lie in-between 1.80 and 2.14 [15,17]. The change from Fabry-Pérot to whispering gallery resonance modes can be attributed to the reduction of the cross section area in the In_2O_3 nanostructures. As observed in their SEM micrographs, the aspect ratio of Ga-incorporated straight nanorods is much higher than tapered-end pristine In_2O_3 nanorods due to their higher growth rate. When the micro-/nanostructures cross section is reduced beyond a threshold value [6,17], the plane wave can no longer be resonant in the cavity due to the similarity between the cavity length and wavelength of photoluminescence emission of the nanorods. As can be observed in the schematic representation of the optical paths (Figs. 8c and 8d), the optical path of Fabry-Pérot (L_{FP}) modes is smaller than that of whispering gallery modes ($L_{WG} = \sqrt{8d^2}$). Thus, on cavity size reduction, the change from Fabry-Pérot to whispering gallery modes can be observed in the nanorods of smaller cross sections. Nevertheless, for specific threshold cavity size both resonant modes can appear, as observed by García-Tecedor et al. [5] in Cr-doped SnO_2 microplates, where the thickness (t) to width (w) ratio threshold value ~0.7 was estimated for the achievement of total internal reflection. In that case, the microplates with t/w ratios below 0.7 revealed Fabry-Pérot modes, while the microplates with t/w ratios above 0.7 exhibited both Fabry-Pérot and whispering gallery modes. As observed by Zimmler et al. [31] in thermally grown ZnO nanowires, there is a strong dependence of the nanowire diameter on the Fabry-Pérot resonant modes. The ZnO nanowires present lasing property only if their diameters are above ~150 nm. Below this size, the ZnO nanowires did not present lasing, irrespective of their lengths.

For applications in optoelectronic devices such as microresonators or lasing microcavities, the quality factor (Q), which is related to the ratio between the stored energy and the dissipated energy in each loop, can be estimated using Eq. (6):

$$Q = \lambda/\Gamma \quad (6)$$

where Γ is the full width at half maximum of the peak at λ. For the pristine nanostructure, the estimated quality factor was 20.86, which is quite low for optical application [17]. Nevertheless, the Q factor for Ga-incorporated nanostructures improved up to 188.79. Such increase in the Q factor can be associated with the increment in the refractive index of the nanostructures due to Ga incorporation, and the reduction of the nanorod roughness. As has been stated earlier, not all the nanostructures revealed waveguiding behavior. However, the Q values estimated for the pristine and Ga-incorporated nanostructures are representative for all nanostructures which present resonance modes, either Fabry-Pérot or whispering-gallery type. Thus, the incorporation of Ga in the In_2O_3 nanostructures not only improves their morphology through enhanced growth rate and surface smoothness, but also enhances their Q factor, making them suitable for use in optical communication systems [32].

4. Conclusions

In summary, we present the fabrication of pristine and Ga-doped nanorods of high aspect ratios with high crystalline quality through VLS growth process. The morphology of In_2O_3 nanostructures evolves from tapered to straight nanorods due to enhanced growth rate induced by Ga incorporation, without significant deterioration in crystal quality. Formation of a few core-shell nanostructures in Ga-incorporated sample clearly indicates a segregation of Ga towards nanorod surface. The waveguiding behavior of the nanorods could be observed when one of their edges was illuminated with a monochromatic He-Ne laser. Furthermore, the fabricated nanostructures revealed Fabry-Pérot and whispering gallery mode resonances, depending on their size and refraction index of the optical cavity, both of which could be tuned by Ga incorporation. Ga incorporation not only enhances the aspect ratio of the In_2O_3 nanorods but also makes their surface smoother, which is helpful to prevent light loss through scattering. The fabrication of high-quality nanostructures in a simple scalable process opens up the door for the development of new optoelectronic devices, such as micro-/nanoresonators, solid-state lasers, and light waveguides.

Acknowledgements

The work was partially supported by VIEP-BUAP, Mexico (Grant # VIEP/EXC/2017-257) and project MAT2015-65274-R (MINECO/FEDER). JARR thanks CONACyT, Mexico, for extending doctoral fellowship (# 279219).

References

[1] B. Yan, L. Liao, Y. You, X. Xu, Z. Zheng, Z. Shen, J. Ma, L. Tong, T. Yu, Single-crystalline V_2O_5 ultralong nanoribbon waveguides, Adv. Mater. 21 (2009) 2436–2440.
[2] R. Dangel, J. Hofrichter, F. Horst, D. Jubin, A. La Porta, N. Meier, I.M. Soganci, J. Weiss, B.J. Offrein, Polymer waveguides for electro-optical integration in data centers and high-performance computers, Optic Express 23 (2015) 4736.
[3] D. Psaltis, R.A. Athale, High accuracy computation with linear analog optical systems: a critical study, Appl. Optic. 25 (1986) 3071.
[4] P. Hidalgo, B. Méndez, J. Piqueras, High aspect ratio GeO_2 nano- and microwires with waveguiding behaviour, Nanotechnology 18 (2007) 155203.
[5] M. García-Tecedor, D. Maestre, A. Cremades, J. Piqueras, Tailoring optical resonant cavity modes in SnO_2 microstructures through doping and shape engineering, J. Phys. D Appl. Phys. 50 (2017) 415104.
[6] E. Nogales, J.Á. García, B. Méndez, J. Piqueras, Doped gallium oxide nanowires with waveguiding behavior, Appl. Phys. Lett. 91 (2007) 133108.
[7] L. Dai, X.L. Chen, J.K. Jian, M. He, T. Zhou, B.Q. Hu, Fabrication and characterization of In_2O_3 nanowires, Appl. Phys. A Mater. Sci. Process 75 (2002) 687–689.
[8] J. Bartolomé, D. Maestre, A. Cremades, M. Amatti, J. Piqueras, Composition-dependent electronic properties of indium–zinc–oxide elongated microstructures, Acta Mater. 61 (2013) 1932–1943.
[9] J. Gao, R. Chen, D.H. Li, L. Jiang, J.C. Ye, X.C. Ma, X.D. Chen, Q.H. Xiong, H.D. Sun, T. Wu, UV light emitting transparent conducting tin-doped indium oxide (ITO) nanowires, Nanotechnology 22 (2011) 195706.
[10] A. El Hichou, M. Addou, M. Mansori, J. Ebothé, Structural, optical and luminescent characteristics of sprayed fluorine-doped In_2O_3 thin films for solar cells, Sol. Energy Mater. Sol. Cells 93 (2009) 609–612.
[11] S. Ju, F. Ishikawa, P. Chen, H.-K. Chang, C. Zhou, Y. Ha, J. Liu, A. Facchetti,

T.J. Marks, D.B. Janes, High performance In_2O_3 nanowire transistors using organic gate nanodielectrics, Appl. Phys. Lett. 92 (2008) 222105.
[12] W.J. Kim, D. Pradhan, Y. Sohn, Fundamental nature and CO oxidation activities of indium oxide nanostructures: 1D-wires, 2D-plates, and 3D-cubes and donuts, J. Mater. Chem. A 1 (2013) 10193–10202.
[13] M. Kumar, V.N. Singh, F. Singh, K.V. Lakshmi, B.R. Mehta, J.P. Singh, On the origin of photoluminescence in indium oxide octahedron structures, Appl. Phys. Lett. 92 (2008) 171907.
[14] D.A. Magdas, A. Cremades, J. Piqueras, Growth and luminescence of elongated In_2O_3 micro- and nanostructures in thermally treated InN, Appl. Phys. Lett. 88 (2006) 14–16.
[15] K. Ozasa, T. Ye, Y. Aoyagi, Deposition of gallium oxide and indium oxide on GaAs for in situ process use by alternating supply of TEGa, TMIn, and H_2O_2 as surge pulses, J. Vac. Sci. Technol. A Vac. Surf. Film 12 (1994) 120–124.
[16] T. Tsuruoka, C.H. Liang, K. Terabe, T. Hasegawa, Optical waveguide properties of single indium oxide nanofibers, J. Opt. A Pure Appl. Opt. 10 (2008) 55201.
[17] J. Bartolomé, A. Cremades, J. Piqueras, Thermal growth, luminescence and whispering gallery resonance modes of indium oxide microrods and microcrystals, J. Mater. Chem. C 1 (2013) 6790.
[18] Y. Yan, Y. Zhang, H. Zeng, J. Zhang, X. Cao, L. Zhang, Tunable synthesis of In_2O_3 nanowires, nanoarrows and nanorods, Nanotechnology 18 (2007) 175601.
[19] J.A. Ramos Ramón, A. Cremades, D. Maestre, R. Silva González, U. Pal, Fabricating necklace-, tower-, and rod-shaped In_2O_3 nanostructures by controlling saturation kinetics of catalyst droplets in a vapor–liquid–solid process, Cryst. Growth Des. 17 (2017) 4596–4602.
[20] R.E. Honig, Vapor pressure data for the more common elements, RCA Rev. A Tech. J. 18 (1957) 195–204.
[21] H.J. Chun, Y.S. Choi, S.Y. Bae, H.C. Choi, J. Park, Single-crystalline gallium-doped indium oxide nanowires, Appl. Phys. Lett. 85 (2004) 461–464.
[22] I. López, A.D. Utrilla, E. Nogales, B. Méndez, J. Piqueras, A. Peche, J. Ramírez-Castellanos, J.M. González-Calbet, In-doped gallium oxide micro- and nanostructures: morphology, structure, and luminescence properties, J. Phys. Chem. C 116 (2012) 3935–3943.
[23] O.M. Berengue, A.D. Rodrigues, C.J. Dalmaschio, A.J.C. Lanfredi, E.R. Leite, A.J. Chiquito, Structural characterization of indium oxide nanostructures: a Raman analysis, J. Phys. D Appl. Phys. 43 (2010) 45401.
[24] D.J. Seo, S.H. Park, Structural, electrical and optical properties of In_2O_3:Mo films deposited by spray pyrolysis, Phys. B Condens. Matter 357 (2005) 420–427.
[25] M.H. Huang, Y. Wu, H. Feick, N. Tran, E. Weber, P. Yang, Catalytic growth of zinc oxide nanowires by vapor transport, Adv. Mater. 13 (2001) 113–116.
[26] C.H. Liang, G. Meng, Y. Lei, F. Phillipp, L. Zhang, Sol-gel growth of In_2O_3 thin films, Adv. Mater. 13 (2001) 1330–1333.
[27] F. Zeng, X. Zhang, J. Wang, L. Wang, L. Zhang, Large-scale growth of In_2O_3 nanowires and their optical properties, Nanotechnology 15 (2004) 596–600.
[28] H. Dong, S. Sun, L. Sun, W. Xie, L. Zhou, X. Shen, Z. Chen, Single-crystalline polyhedral In_2O_3 vertical Fabry–Pérot resonators, Appl. Phys. Lett. 98 (2011) 11913.
[29] J.C. Knight, G. Cheung, F. Jacques, T.A. Birks, Phase-matched excitation of whispering-gallery-mode resonances by a fiber taper, Opt. Lett. 22 (1997) 1129.
[30] R.J. Cava, J.M. Phillips, J. Kwo, G.A. Thomas, R.B. van Dover, S.A. Carter, J.J. Krajewski, W.F. Peck, J.H. Marshall, D.H. Rapkine, $GaInO_3$: a new transparent conducting oxide, Appl. Phys. Lett. 64 (1994) 2071–2072.
[31] M.A. Zimmler, J. Bao, F. Capasso, S. Müller, C. Ronning, Laser action in nanowires: observation of the transition from amplified spontaneous emission to laser oscillation, Appl. Phys. Lett. 93 (2008) 51101.
[32] D.J. Gargas, M.C. Moore, A. Ni, S.-W. Chang, Z. Zhang, S.-L. Chuang, P. Yang, Whispering gallery mode lasing from zinc oxide hexagonal nanodisks, ACS Nano 4 (2010) 3270–3276.